Supplementary Information for

Carbon-based manufacturing for flexible terahertz metasurfaces

Minghui Deng[1,†], Cheng Gong[1,†,*], Huizhang Zhao[1,3], Huiqi Jiang[1,3], Songjian Li[2], Xiaobing Xie[2], Xian Guo[3], Nan Zhang[1], Jierong Cheng[1], Fei Fan[1], Shengjiang Chang[1]

[1] Institute of Modern Optics, Nankai University, Tianjin, 300350, China.
[2] Hebei Key Laboratory of Compact Fusion, Langfang 065001, China.
[3] Academy for Advanced Interdisciplinary Studies, Nankai University, Tianjin, 300350, China.

†These authors contributed equally to this work.
*gongcheng@nankai.edu.cn

S1 Supplementary information for the preparation of carbon-based ink

Three different carbon-based inks were formulated based on three distinct carbon nanomaterials: carbon black (CB), graphene, and graphene oxide (GO). To achieve optimal printability for the dual-mode (Ink-jet/E-jet) printing system, each ink was prepared with a ternary solvent system comprising terpineol, ethanol and polyester resin as organic binder, dispersing agent and rheological modifier.

After mixing the carbon nanomaterials with the solvent through ice-bath ultrasonication combined with mechanical stirring for one hour, the resulting inks were molded into 30 mm × 8 mm block samples, and sintered at 120 ℃ for 15 min. Then measure the sheet resistance of the samples using a four-point probe resistance meter. Specific formulations and electrical properties of the inks are described as followeds.

1.1 Preparation of the CB-based ink

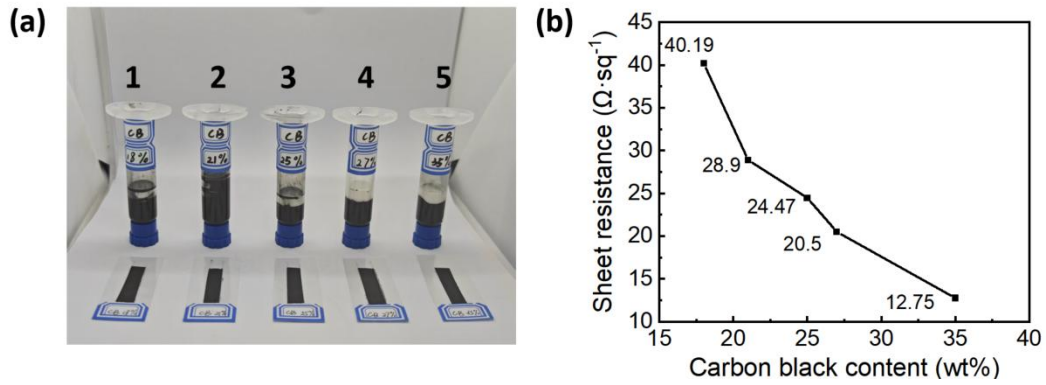

Figure S1 (a) Photograph of CB-based inks and block samples; (b) Sheet resistance curve for different weight percentages of carbon black powder in inks.

Table S1 Formulations and sheet resistances R_s of CB-based inks.

Group	Carbon black (wt%)	Terpineol (wt%)	Ethanol (wt%)	Polyester resin (wt%)	R_s ($\Omega \cdot sq^{-1}$)
1	0.184	0.592	0.066	0.158	40.19
2	0.214	0.535	0.059	0.188	28.9
3	0.253	0.47	0.052	0.226	24.47
4	0.268	0.45	0.05	0.232	20.5
5	0.349	0.314	0.035	0.302	12.75

As shown in Figure S1(a), five samples of CB-based ink are prepared, and the measured result of their sheet resistance is demonstrated in Figure S1(b).

The sheet resistance of the ink decrease as the weight percentage of the carbon black powder in the ink rises. The specific formulations of the inks are shown in Table S1.

1.2 Preparation of the Graphene-based ink

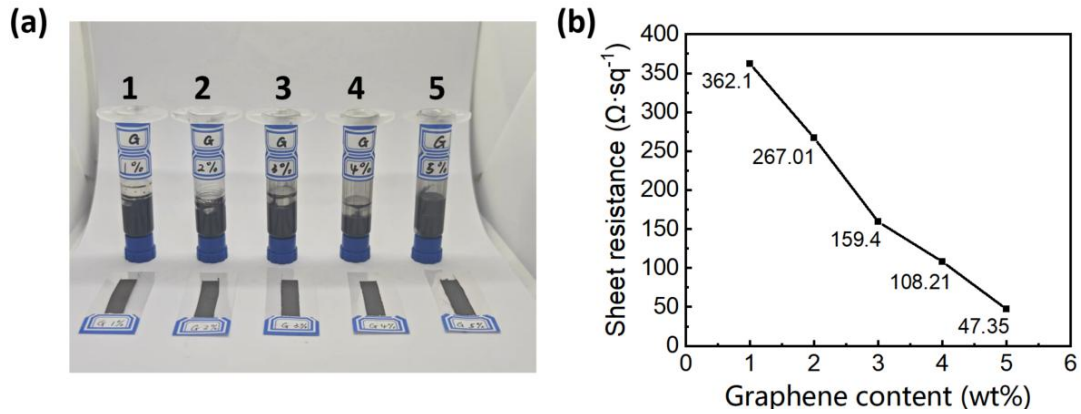

Figure S2 (a) Photograph of graphene-based inks and block samples; (b) Sheet resistance curve for different weight percentages of graphene powder in inks.

Table S2 Formulations and sheet resistances R_s of graphene-based inks.

Group	Graphene (wt%)	Terpineol (wt%)	Ethanol (wt%)	Polyester resin (wt%)	R_s ($\Omega \cdot sq^{-1}$)
1	0.05	0	0	0.95	362.1
2	0.04	0.175	0.0175	0.768	267.01
3	0.03	0.3	0.03	0.64	159.4
4	0.02	0.52	0.058	0.403	108.21
5	0.01	0.418	0.046	0.526	47.35

As shown in Figure S2(a), five samples of graphene-based ink are prepared, and the measured result of their sheet resistance is demonstrated in Figure S2(b). The sheet resistance of the ink decreases as the weight percentage of the graphene powder in the ink rises. The specific formulations are shown in Table S2.

1.3 Preparation of the GO-based ink

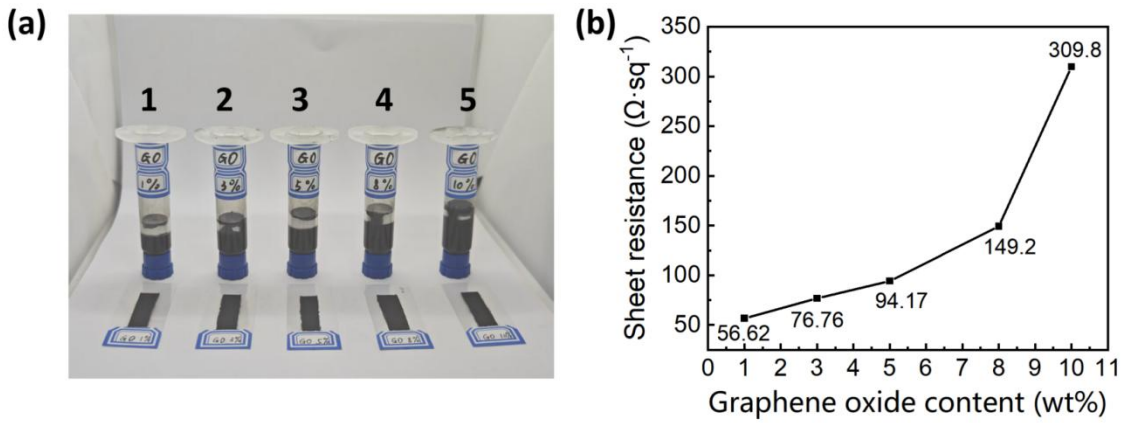

Figure S3 (a) Photograph of GO-based inks and block samples; (b) Sheet resistance curve for different weight percentages of graphene oxide powder in inks.

Table S3 Formulations and sheet resistances R_s of GO-based inks.

Group	Graphene Oxide (wt%)	Carbon black (wt%)	Terpineol (wt%)	Ethanol (wt%)	Polyester resin (wt%)	R_s ($\Omega \cdot sq^{-1}$)
1	0.01	0.293	0.4	0.044	0.253	56.62
2	0.03	0.287	0.392	0.040	0.261	76.76
3	0.05	0.245	0.449	0.045	0.211	94.17
4	0.08	0.216	0.464	0.047	0.193	149.2
5	0.1	0.212	0.456	0.050	0.182	309.8

As shown in Figure S3(a), five samples of GO-based ink are prepared, and the measured result of their sheet resistance is demonstrated in Figure S3(b). It should be noted that graphene oxide differs from carbon black and graphene, exhibiting insulating properties at room temperature. To modulate the initial sheet resistance of GO-based ink, carbon black powder was incorporated during formulation. As a result, the sheet resistance of the GO-based ink increased with the weight percentage of graphene oxide. The specific formulations are shown in Table S3.

S2 Supplementary information for printing mode switching

The printing system can operate in either single-head or dual-head. In the single-head operation mode, the operation is relatively simple. There is no need

to replace the print head; only one print head is used for printing. In dual-head hybrid printing, the print head needs to be switched. The nozzle is a key component of the print head, and its inner diameter is one of the key factors controlling the printing flow. The nozzle can be replaced according to actual circumstances. After each switch, the platform needs to be recalibrated.

Here, we have supplemented relevant details as follows: The two printing heads are fixed onto the displacement stage by a support frame and move independently under the control of two precise stepper motors to extrude carbon-based materials. The system can print two different materials and achieve different printing accuracies according to different printing modes (Ink-jet printing and E-jet printing). The specific operation steps of switching the print head are shown in Figure S4. For ease of description, the print head for the Ink-jet printing is denoted as print head 1, and the print head for the E-jet printing as print head 2:

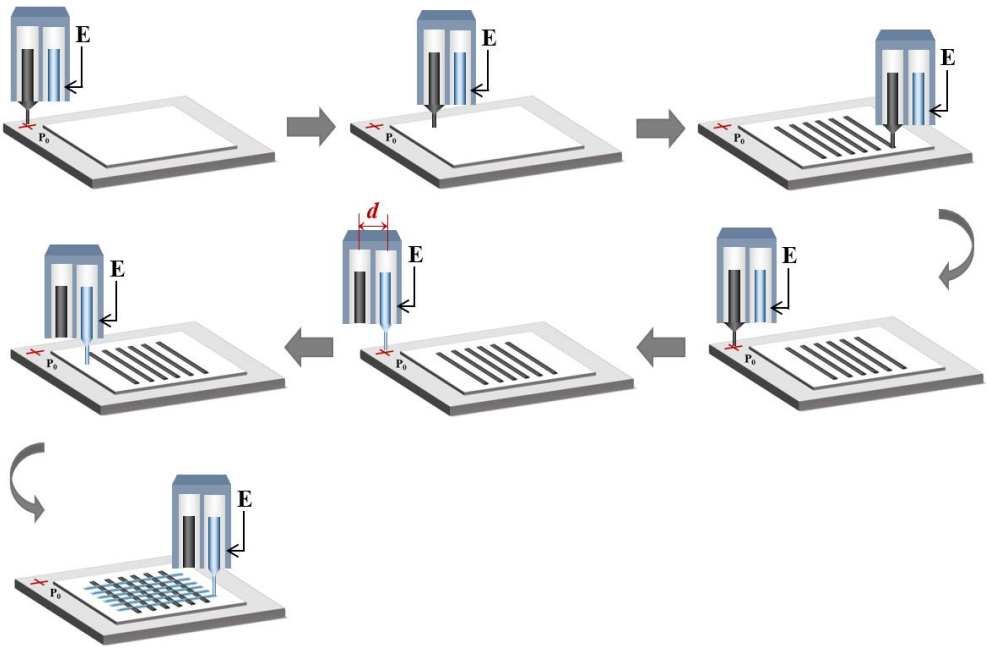

Figure S4 Schematic diagram of specific operation steps for switching print heads.

(1) Position print head 1 at P_0 as a reference point and record its position in the printing system;
(2) Move print head 1 from P_0 to the printing point on the substrate and commence printing;
(3) After printing, reposition print head 1 to P_0;
(4) Perform print head 1 alignment test. If deviation occurs, repeat step (3) for alignment testing until the requirement is met;
(5) Calculate the offset *d* between the two print heads (determined by the dimensions of the 3D-printed frame) and position print head 2 at P_0;
(6) Move print head 2 from point P_0 to the corresponding print point on the substrate, and print the remaining pattern;

(7) Printing completes.

S3 Supplementary information for the determination of printing parameters

For most printing applications, the suitable viscosity range of the ink is 1-10,000 cps[1]. However, the specific printing applications have different requirements for the viscosity of the ink. During ink preparation, we need to adjust the ratio of binder and dispersant to ensure the printability of the ink. At the same time, before printing the metasurface structures, we must conduct printing parameter studies for each type of ink.

To shorten the experimental period for finding the optimal printing parameters, the orthogonal experimental design (OED) method was adopted in this study. The principle of OED is to select a balanced set of representative combinations from the full factorial experiment containing all factors and levels. This approach significantly reduces the number of experiments while ensuring the validity of the data. For example, in an experiment with three factors and three levels, as illustrated by the blue dots in Figure S5(a), a full factorial design would theoretically require $3^3 = 27$ cross-combinations. However, by using the OED, it is only necessary to select representative experiments with uniformly distributed factors, as shown by the red dots in Figure S5(a), which reduces the number of experiments to nine.

The specific experimental process is illustrated in Figure S5(b) and mainly includes the following steps:

(1) Preparation of functional ink: First, according to the electrical property requirements, functional ink suitable for printing is prepared following a specific formula and process;

(2) Determination of printing parameter range: Based on the intrinsic properties of the ink, such as viscosity and surface tension, the preliminary value ranges for each parameter are determined, including nozzle size, feeding rate, printing speed, and applied voltage;

(3) Design of factor-level table: The number of factors is determined based on the number of parameters, and different level values are set for each parameter. Through the factor-level table, each factor and its levels are systematically organized;

(4) Generation of orthogonal experimental design table: Based on the factor-level table, an orthogonal experimental design method is employed to formulate a scientific experimental plan. The orthogonal experimental design table can investigate the influence of multiple factors on the experimental results with fewer experiments, thereby improving experimental efficiency;

(5) Establishment of correspondence between printing parameters and line width: Actual printing experiments are conducted according to the orthogonal experimental design table, and the line width obtained under each set of parameter conditions is measured. Subsequently, based on the line width

required for the structure, the exact printing parameters are further selected.

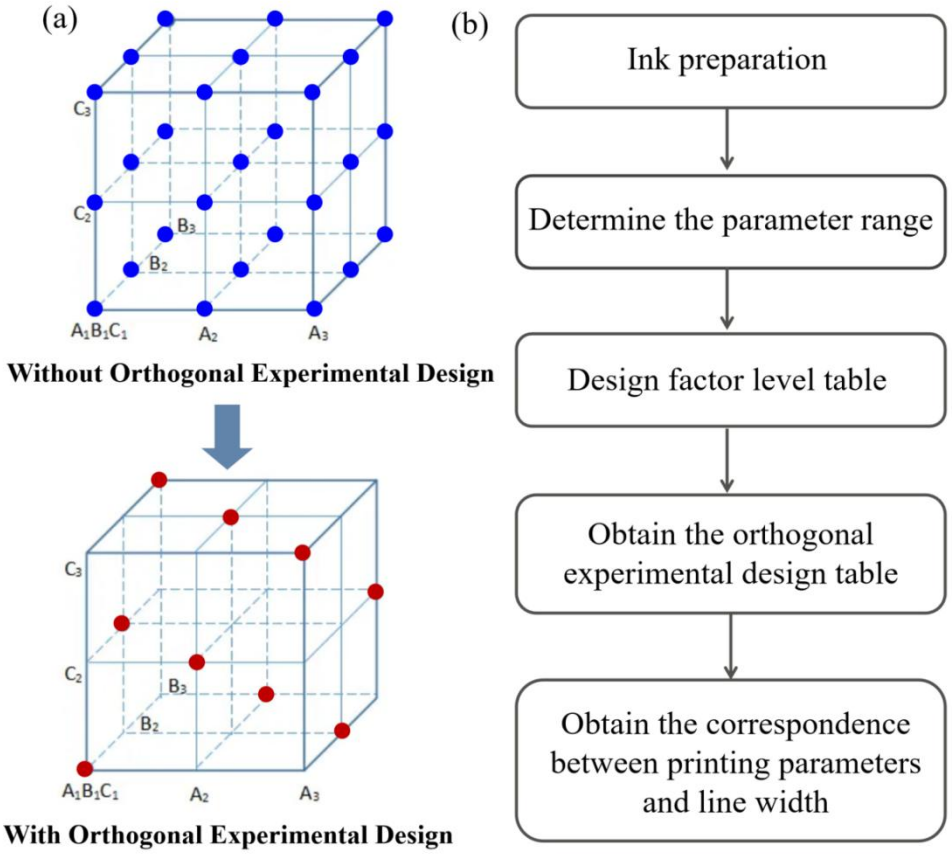

Figure S5 (a) Schematic diagram of the number of experiments without and with orthogonal experimental design method; (b) Flowchart of printing parameter study.

Here, we take the E-jet printing of the CB-based ink mentioned in the manuscript as an example to provide a detailed explanation to the reviewer. This study investigated three factors, feeding rate, moving speed and applied voltage and each at five levels. Conducting a full factorial experiment would theoretically require $5^3 = 125$ experiments, which would consume a significant amount of time and materials. By employing the orthogonal experimental design method, we only needed to design the factor-level table as shown in Table S4.

Table S4 Factor level table.

Factor	Level				
Feeding rate (μm·s^{-1})	0.248	0.496	0.744	0.992	1.24
Moving speed (mm·s^{-1})	10	12.5	15	17.5	20
Voltage (kV)	2.4	2.5	2.6	2.7	2.8

According to Table S4, orthogonal experiments were established with 25 sets of parameter combinations, and the corresponding line widths were

obtained, as shown in Table S5. Based on this, the correspondence between the three printing parameters and the line width for this ink can be rapidly established. Subsequently, according to the line width required for the structure, the exact printing parameters can be further selected.

Table S5 Orthogonal experimental table and test results.

	Feeding rate ($\mu m \cdot s^{-1}$)	Moving speed ($mm \cdot s^{-1}$)	Voltage (kV)	Line width (μm)
1	0.248	10	2.4	155.13
2	0.248	12.5	2.5	132.7
3	0.248	15	2.6	119.23
4	0.248	17.5	2.7	80.21
5	0.248	20	2.8	55.13
6	0.496	10	2.5	151.74
7	0.496	12.5	2.6	125.61
8	0.496	15	2.7	153.93
9	0.496	17.5	2.8	94.77
10	0.496	20	2.4	165.59
11	0.744	10	2.6	137.27
12	0.744	12.5	2.7	110.53
13	0.744	15	2.8	108.72
14	0.744	17.5	2.4	133.52
15	0.744	20	2.5	114.17
16	0.992	10	2.7	126.01
17	0.992	12.5	2.8	124.43
18	0.992	15	2.4	152.77
19	0.992	17.5	2.5	128.3
20	0.992	20	2.6	104.23
21	1.24	10	2.8	172.68
22	1.24	12.5	2.4	169.2
23	1.24	15	2.5	143.86
24	1.24	17.5	2.6	99.03
25	1.24	20	2.7	100.96

Reference:

[1] Yin Z, Wang D, Guo Y, Zhao Z, Li L, Chen W et al. Electrohydrodynamic printing for high resolution patterning of flexible electronics toward industrial applications. Info Mat 2024; 6: e12505.

S4 Supplementary information for the printing parameters of metasurface samples

The printing parameters for each metasurface sample are presented in Table S6.

Table S6 Printing parameters of the metasurfaces in the manuscript

Metasurface	Nozzle size (mm)	Feeding rate (μm·s^{-1})	Moving speed (mm·s^{-1})	Voltage (kV)
Paper-based metasurface absorber	0.21	0.248	12.5	2.8
PET-based metasurface absorber	0.36	0.992	20	0
Metasurface filter	0.21	0.248	20	2.6

S5 Supplementary information for substrate roughness and ink penetration

To provide a more profound explanation for why the measured absorption bandwidth of the paper-based absorber is broader than the simulated results, the roughness of the substrates and the ink penetration morphology were characterized.

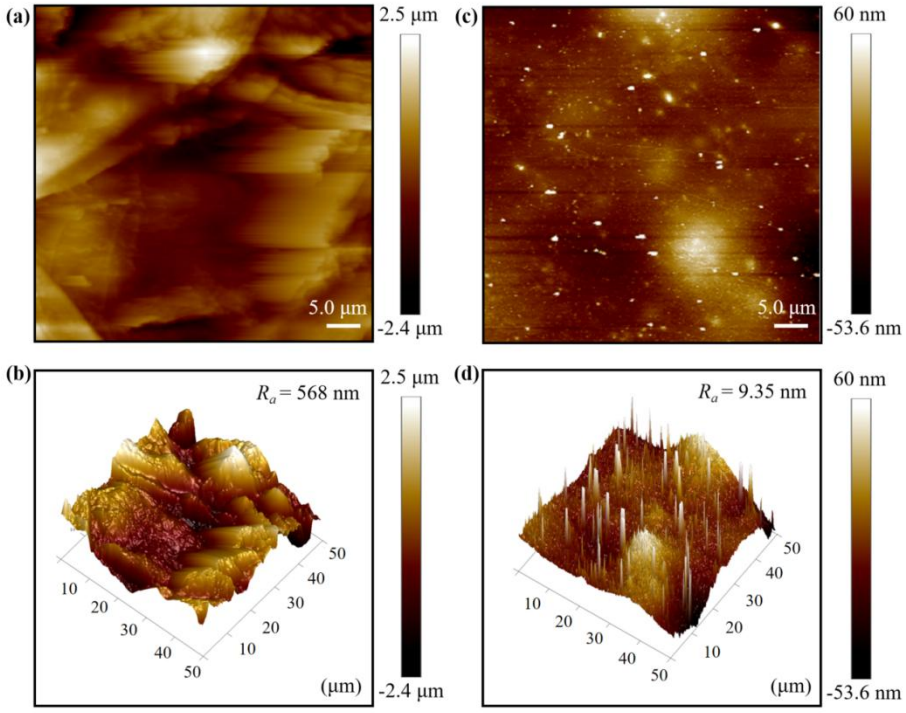

Figure S6 AFM images: (a) Plan view of paper surface; (b) Stereoscopic view of

paper surface; (c) Plan view of PET surface; (d) Stereoscopic view of PET surface.

Firstly, atomic force microscopy (AFM) measurements were conducted on the blank paper substrate and blank PET film used in the experiments. Figure S6 shows the measurement results for a 50 μm × 50 μm area. The root mean square roughness (R_q) of PET is 14.3 nm, and the arithmetic average roughness (R_a) is 9.35 nm; the R_q of paper is 695 nm, and the R_a is 568 nm. Due to the intertwined fibrous structure, the roughness of paper is significantly greater than that of PET.

Secondly, to visualize the penetration morphology of the ink on the paper surface, we also performed high-magnification microscopic imaging of the cross-section of the patterned paper substrate, as shown in Figure S7(a). Figure S7(b) presents the microscopic imaging result, revealing that the ink penetrated approximately 30 μm into the paper.

Combining the high roughness of the paper measured by AFM with the ink penetration morphology observed under the microscope provides a more profound explanation for why the measured absorption bandwidth of the paper-based absorber is broader than the simulated results: The microscopic unevenness of the paper surface and the vertical penetration of the ink introduce complex variations in the resonance.

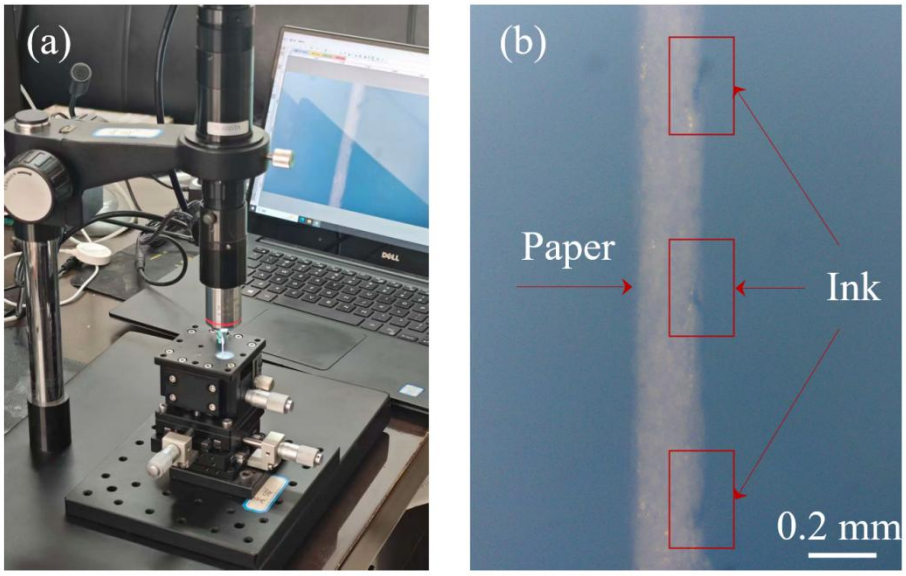

Figure S7 (a) Photo of the microscopic imaging setup; (b) Micrograph of the ink penetration morphology.

S6 Supplementary information for device performance characterizations in oblique incidence

It is insufficient to demonstrate flexibility only through photographs; for the practical application of flexible devices, quantitative evaluation of their performance stability under bent state is crucial. When a flexible metasurface conforms to a non-planar surface, localized regions of the metasurface will be in a bent state, causing the incident angle of the terahertz wave relative to the metasurface to change. Therefore, by measuring the spectral response of the device under different incident angles, the performance variation under bending can be equivalently characterized. Based on this approach, we have supplemented the simulation and measurement results of the metasurfaces under oblique incidence conditions, thereby evaluating their performance stability in practical application scenarios.

6.1 Absorbing metasurface

Figure S8(a) presents the simulated absorption A of the paper-based metasurface absorber under different incident angles. As the incident angle gradually increases, the absorption band shifts toward higher frequencies, accompanied by a decrease in amplitude. Figure S8(b) shows the simulated absorption A of the PET-based metasurface absorber under different incident angles. As the incident angle increases, the absorption peak exhibits a slight blue shift and broadening.

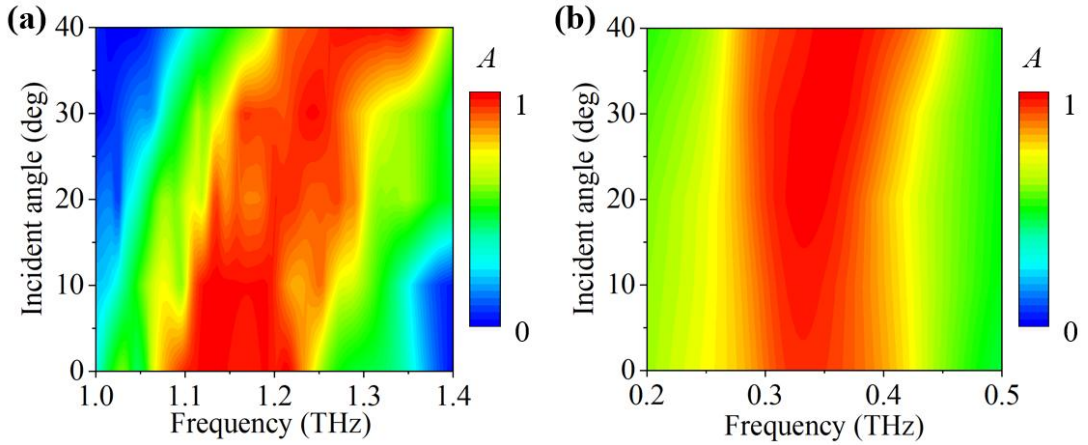

Figure S8 Simulated absorption at different incident angles ranging: (a) Paper-based metasurface absorber; (b) PET-based metasurface absorber.

As shown in Figure S9(a), we utilized the turntable in the THz-TDS system to adjust the angle between the emitting and receiving antennas, thereby varying the incident angle θ and measuring the reflection R at different incident angles. Due to the limitations of the experimental setup, we measured the cases with incident angles ranging from 20° to 40°. Since the terahertz wave transmission is suppressed by the ground layer ($T \approx 0$), the absorption was calculated using the formula $A = 1\text{-}R\text{-}T$.

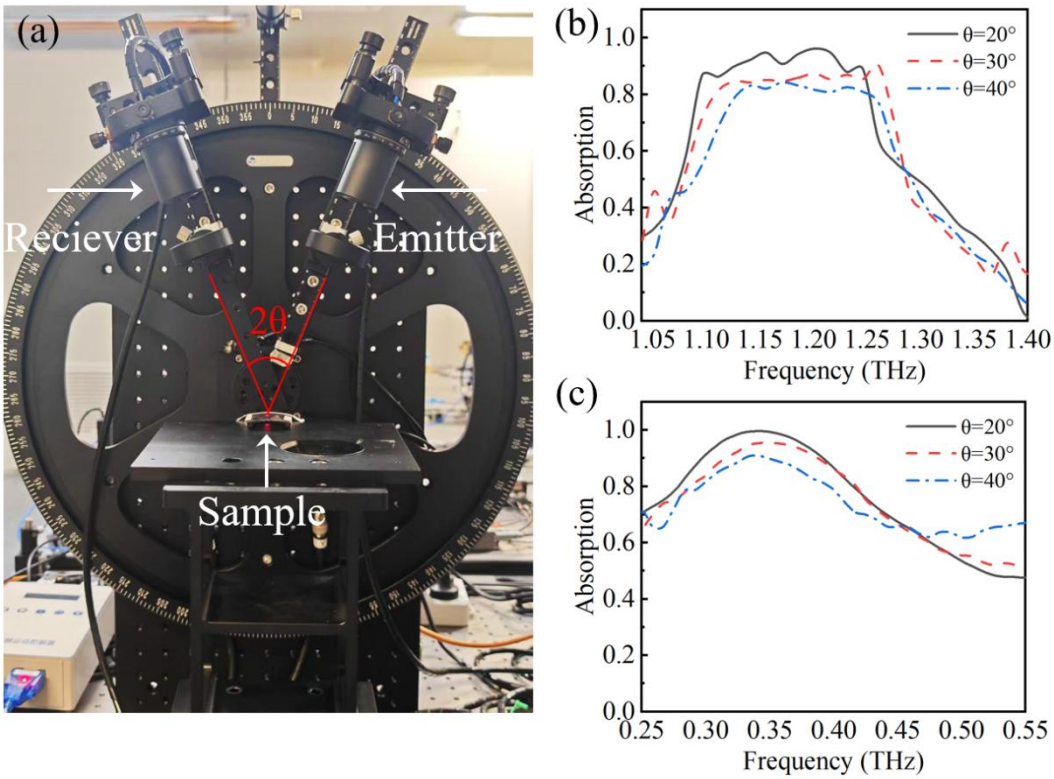

Figure S9 (a) Photograph of the experimental setup for reflection measurement at different incident angles; (b) Measured absorption of the Paper-based metasurface absorber under different incident angles; (c) Measured absorption of the PET-based metasurface absorber under different incident angles.

The measured absorption results for the paper-based metasurface absorber are shown in Figure S9(b). When the incident angle θ increased from 20° to 40°, the overall amplitude of the absorption band decreased, accompanied by a shift of the band position toward higher frequencies. This trend is generally consistent with the simulation results. The measured absorption results for the PET-based metasurface absorber are shown in Figure S9(c). As the incident angle θ increased from 20° to 40°, the amplitude of the absorption peak decreased, while the peak position shifted toward higher frequencies, showing good agreement with the simulation results. This validates the operational stability of the devices under oblique incidence conditions.

6.2 Metasurface filter

For the metasurface filter, we also conducted an incident-angle-dependent study of its transmission. As shown in Figure S10(a), by simultaneously rotating the emitting and receiving antennas in the THz-TDS system while keeping them parallel and rotating at the same angle θ, terahertz waves were incident onto the sample surface at different angles θ, and the transmission response was measured.

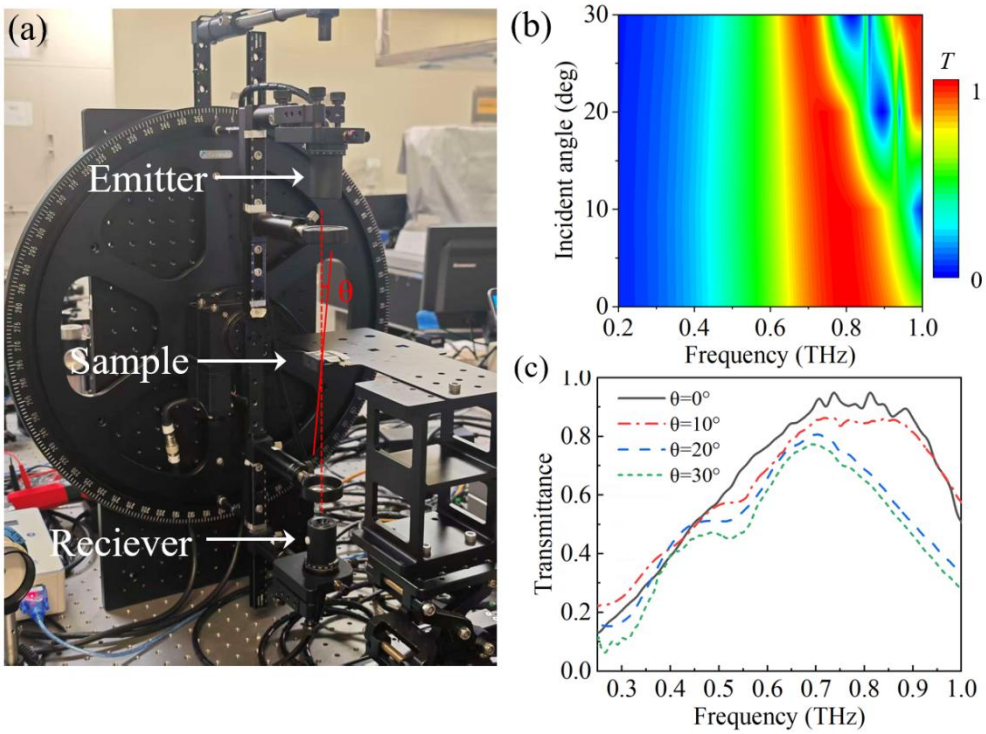

Figure S10 (a) Photograph of the experimental setup for transmission measurement at different incident angles; (b) Simulated transmission under different incident angles; (c) Measured transmission of the metasurface filter under different incident angles.

Figure S10(b) presents the simulated transmission T of the metasurface filter under different incident angles. As the incident angle increased from 0° to 40°, the centre frequency of the transmission peak remained stable, indicating that the device maintains good filtering characteristics over a wide angular range. The measured transmittance results are shown in Figure S10(c). As the incident angle increased, the centre frequency of the transmission peak gradually shifted toward lower frequencies, accompanied by a reduction in bandwidth. Furthermore, when the incident angle exceeded 30°, a second transmission peak began to emerge at higher frequencies, indicating that large-angle incidence excites a higher-order mode transmission response. Nevertheless, the metasurface still maintained satisfactory filtering functionality within an incident angle range of up to 30°, validating its practicality under oblique incidence conditions.

S7 Supplementary information for comparison with other fabrication technologies

We present a simple comparison between this technology and traditional semiconductor processing techniques, as shown in Table S7. It can be seen that

compared to typical semiconductor processes, this approach offers a faster, simpler, and more cost-effective route for fabricating carbon-based terahertz metamaterials. Its low equipment investment facilitates large-scale production, while short preparation cycles make it ideal for rapid iteration.

Table S7 Comparison between this technology and traditional semiconductor processing techniques.

Methods	**Lithography & Etching & Coating**	**Nano imprinting**	**Direct laser writing**	**This work**
Cost	High	High	High	Low
Time	Long	Medium	Medium	Short
Equipment footprint	Large	Large	Large	Small
Process complexity	Complex	Medium	Medium	Simple
Compatibility of substrate material	Limited	Not limited	Limited	Not limited
Compatibility of carbon-based material	Limited	Limited	Limited	Not limited
Large-area fabrication	Limited	Not limited	Not limited	Not limited
Precision	Micro & Nano-scale	Micro & Nano-scale	Micro & Nano-scale	Micro-scale

Besides, we also compared the proposed terahertz metasurfaces with other printed terahertz metasurfaces in terms of device performance and manufacturing method, as shown in Table S8. It can be seen that the technique proposed in this paper can achieve performance comparable to existing terahertz printed devices, and offers advantages such as high speed, compact size, and high integration.

Table S8 Comparison with other printed terahertz metasurfaces in device performance and manufacturing method.

Ref.	**Device Performance**		**Manufacturing method and system**				
	Performance	**Flexible?**	**Key Processes**	**Printing mode**	**Complexity**	**Speed**	**Equipment Integration**
[1]	Absorption >90% @0.31 THz	No	Two-photon Printing & Magnetron Sputtering	Single	High	Slow	Large
[2]	Absorption >90% @0.48 THz	No	Electrohydrodynamic printing	Single	Low	Fast	Small
[3]	Band-stop	No	Electrohydrodynamic	Single	High	Slow	Large

	1.1% @0.519 THz		printing & Mask-patterned etching				
[4]	Absorption >90% @0.08~0.11 THz	Yes	Digital Light Processing 3D printing	Single	Low	Fast	Small
[5]	Absorption >90% @0.7~1.4 THz	Yes	Ink-jet printing	Single	Low	Fast	Small
[6]	Absorption >90% @1.16~1.63 THz	Yes	Ink-jet printing	Single	Low	Fast	Small
This work	**Absorption >90% @ 1.12~1.245 THz Absorption >90% @ 0.295~0.39 THz Transmission >90% @0.8 THz**	**Yes**	**Ink-jet printing E-jet printing**	**Two**	**Low**	**Fast**	**Small**

References:

[1] Chen X, Ye L, Yu D. Terahertz sensing with a 3D meta-absorbing chip based on two-photon polymerization printing. Photonics Res 2024; 12: 895.

[2] Gong H, Huang J, Wang J, Zhao P, Guo M, Liang C et al. Additive Manufacturing for Terahertz Metamaterials on the Dielectric Surface based on Optimized Electrohydrodynamic Drop-on-demand Printing Technology. ACS Appl Mater Interfaces 2024; 16: 4222–4230.

[3] Wang J, Gong H, Huang J, Zhang J, Zhao P, Zhang Q et al. Patterned mask etching enhanced electrohydrodynamic printing for terahertz metasurfaces. APL Photonics 2025; 10: 120801.

[4] Y.R. Wang, R.Y. Su, J.Y. Chen, W.Q. Wang, X.Q. Zhang, H. Xu, R.J. He, 3D Printed Bioinspired Flexible Absorber: Toward High-Performance Electromagnetic Absorption at 75−110 GHz. ACS Appl. Mater. Interfaces 2023; 15: 53996-54005.

[5] Huang W, Liu X, Zhou Y, Yang S, Huang W, Chen Z et al. Inkjet-Printing $Ti_3C_2T_x$ MXene Nanosheet-Based Metamaterials for Terahertz Absorption. ACS Appl Nano Mater 2024; 7: 15308–15316.

[6] Niu J, Chao X, Lian H, Luo J, Qi L. Machine learning and droplet-based printing accelerating the achievement of flexible terahertz metamaterial absorber. Chemical Engineering Journal 2025; 519: 165123.

S8 Supplementary information for sintering temperature and sintering time

The sintering temperature and time have a significant impact on the performance of carbon-based thin film materials. If the temperature is too low or the time is too short, residual solvent and adhesives in the ink will remain,

resulting in high sheet resistance and insufficient adhesion. If the temperature is too high or the time is too long, the carbon-based materials will become brittle and crack. At the same time, the temperature tolerance of the substrate also limits the sintering temperature and time. If the temperature is too high or the time is too long, the flexible substrate material will be curled, warped or even permanently deformed. Next, we will make a detailed analysis:

(1) Substrate Thermal Stability

For the two types of PET films used in the experiments, the maximum withstand temperature is 150 °C. For the paper substrate, excessive heating can cause it to become brittle, yellow, or even carbonize. Therefore, to ensure that the substrate material does not deform or degrade during sintering, we controlled the sintering temperature below 150 °C. The 120 °C is a safe and efficient temperature point in the experiment.

(2) Boiling Points of the Solvent System

The composite solvent system contains terpineol (boiling point approximately 214-217 °C) and ethanol (boiling point 78.23 $\pm$ 0.09 °C). Sintering at 120 °C can effectively and rapidly evaporates the ethanol and slowly volatilizing the terpineol and some components of the organic binder (polyester resin).

Therefore, considering the above two factors comprehensively, we set the sintering temperature to 120 °C. We observed in the experiments that sintering at 120 °C for 15 minutes ensures good electrical conductivity while maintaining sufficient flexibility of the material, enabling it to withstand repeated bending without deformation.

S9 Supplementary information for fabrication repeatability and uniformity

9.1 Fabrication repeatability

To evaluate the repeatability of the manufacturing process, we conducted repeated experiments using the same set of printing parameters and characterized the printed line width.

For the Ink-jet mode, two independent samples were fabricated using the same parameters (feeding rate: 0.744 μm·s^{-1}, moving speed: 20 mm·s^{-1}, nozzle size: 0.21 mm), and their printing effects are shown in Figure S11(a). To quantitatively assess the consistency of the line width, four representative printed lines were selected from the central region of each sample. For each line, the line width was measured at ten uniformly distributed positions, and the average value was taken as the characteristic line width of that line. The statistical results are presented in Figure S11(b). The experiments indicate that the relative standard deviation (RSD) of the line width measurements for the two samples printed with the same parameters is less than 5%, demonstrating good

repeatability and stability of the Ink-jet printing mode.

For the E-jet mode, two independent samples were also fabricated using the same parameters (feeding rate: 0.248 μm·s^{-1}, printing speed: 20 mm·s^{-1}, nozzle inner diameter: 0.21 mm, applied voltage: 2.4 kV), and their printing effects are shown in Figure S11(c). The line width was characterized using the same method, and the statistical results are presented in Figure S11(d). The relative standard deviation (RSD) of the line width measurements is less than 5%, demonstrating good repeatability and stability of the E-jet printing mode.

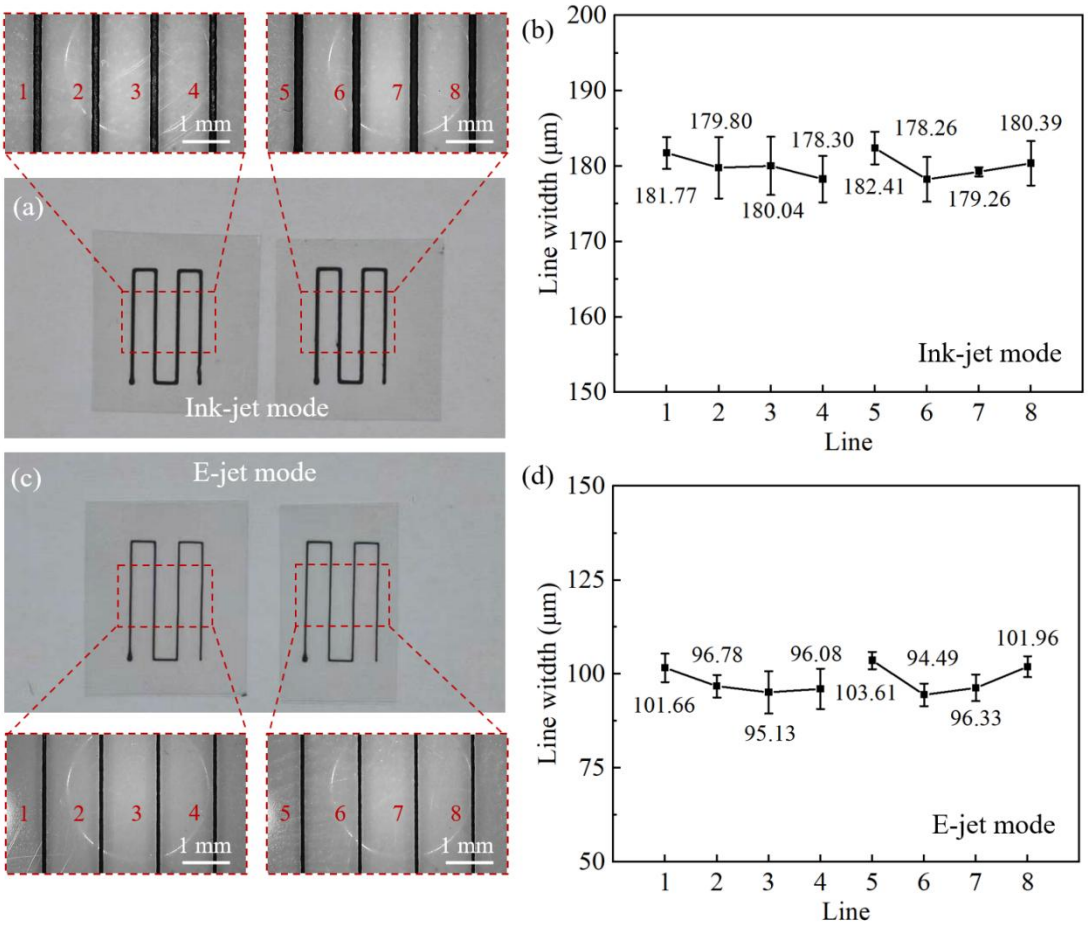

Figure S11 Ink-jet printed samples: (a) Macroscopic photograph and Micrograph; (b) Line width measurement results. E-jet printed samples: (c) Macroscopic photograph and Micrograph; (d) Line width measurement results.

9.2 Fabrication uniformity

To evaluate the uniformity of the printed patterns, we performed multi-point line width measurement analysis in different areas for each sample. As shown in Figure S12(a), nine characteristic positions were uniformly selected as measurement points within the patterned region of each sample. The measurement results are presented in Figure S12(b). The relative standard deviation (RSD) values of the line width measurements for the three samples are

5.25%, 3.68%, and 1.90%, respectively, demonstrating uniformity. Notably, for the PET-based metasurface absorber, the line widths at position 1 and position 2 were slightly higher than the average. Through experimental observation and analysis, this is mainly due to the accumulation of ink during the initial printing process. In subsequent fabrication, this issue can be optimized by adding a brim structure around the printed pattern. Specifically, printing the brim first stabilizes the ink jet before proceeding to the main pattern printing, thereby effectively eliminating line width fluctuations during the initial stage.

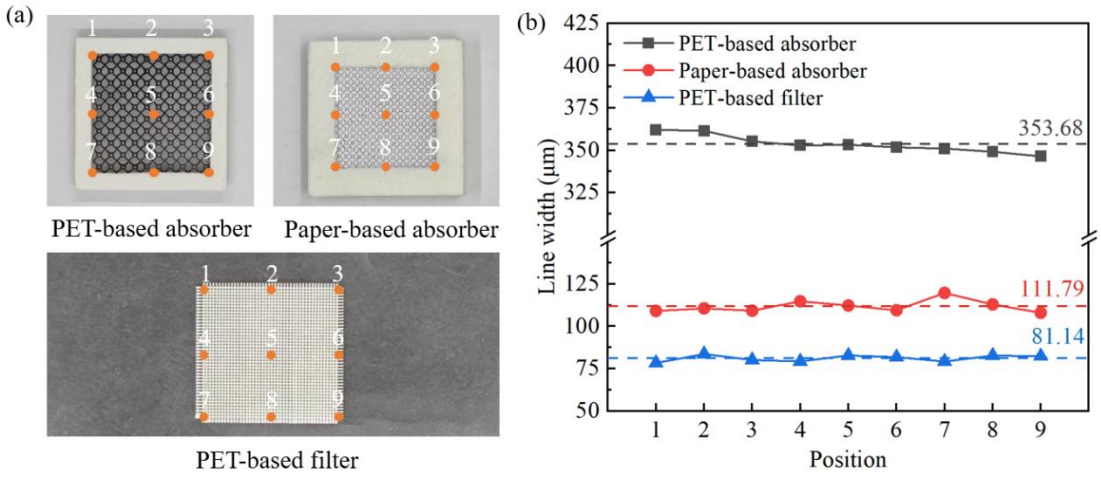

Figure S12 (a) Schematic diagram of measurement points distribution for printing uniformity evaluation; (b) Line width measurement results at each measurement points.

S10 Supplementary information for adhesion and conductivity of bent material

For the practical application of the devices, quantitative evaluation of their performance under bent state is crucial. We observed the micro-structures under different bending states and used microscopy to characterize their adhesion performance.

Firstly, bend the printed lines several times at an angle θ, as shown in Figure S13 (a), to test its adhesion and electoral continuity. Figure S13(b,c) presents micrographs of the same position under the initial state and after 20 bending cycles at an angle of approximately 60°. It can be observed that the material remains well adhered after repeated bending, with no significant delamination or cracking. Furthermore, we measured the electrical properties of the printed lines before and after bending. In the initial state, the sheet resistance of the lines was 126.4 $\Omega \cdot sq^{-1}$, and after bending, the sheet resistance at the same position was 131.6 $\Omega \cdot sq^{-1}$, indicating that the electrical continuity of the lines remains well maintained.

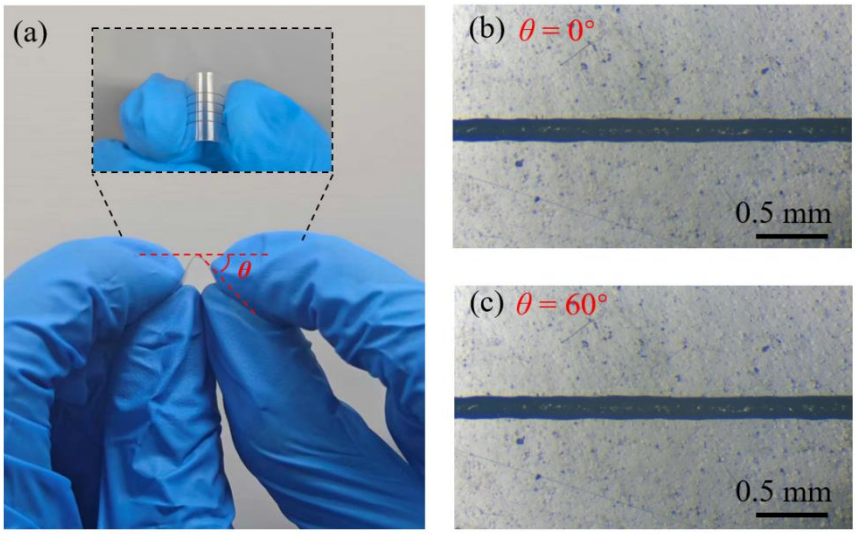

Figure S13 (a) Schematic diagram of the bending test; (b) Micrograph of the initial state; (c) Micrograph after 20 cycles of 60° bending.